# Numerical and Experimental Investigation of Wingtip-Mounted Propellers

**Clément Nardari [(1)] and Rafael Ihi[(2)]**
[(1)] *A&D/eVTOL Industry Expert, Dassault Systemes SIMULIA, Boston, MA, USA, clement.nardari@3ds.com*
[(2)] *Industry Process Consultant, Dassault Systemes SIMULIA, São Paulo, Brazil, rafael.ihi@3ds.com*

## ABSTRACT

This paper presents the computational results of SIMULIA PowerFLOW[®] compared to the experimental investigation provided at the 1st AIAA Workshop for Integrated Propeller Prediction (WIPP). Due to the renewed and growing interest in eVTOL aircraft and limited publicly available experiments, this workshop provided integrated propeller data for assessment of computational tools. The objective of the workshop was to provide open-access wind tunnel data to evaluate wingtip-mounted propellers. Understanding this complex aerodynamic interaction is essential to improve wingtip-mounted propeller design. In order to reduce design time and development cost for this type of vehicle configuration, accurate computational tools are required. These tools will need to capture the complex unsteady flow interactions to optimize the wing-propeller aerodynamic integrated design. However, the accuracy of these tools must first be established. Therefore, PowerFLOW simulations are performed and compared to experimental measurements of wing surface pressure, lift, drag and thrust coefficients. Predication accuracy for wing-propeller interaction is demonstrated by comparing different propeller RPM and wing angle of attack with and without the wingtip-mounted propeller. In addition, experimental measures are limited due to the intrusiveness of the measurement which can lead to a lack of understanding in the physics of the flow and impact the overall wing-tip-mounted propeller performance. Therefore, PowerFLOW unsteady simulations yield insight of propeller-wing wake interactions to better understand the aerodynamic efficiency benefits of a wingtip-mounted propeller.

## 1. NOMENCLATURE

BL      boundary layer
c       chord
CDWA        drag coefficient "Wind axis"
CLWA        lift coefficient "Wind axis"
$C_p$      pressure coefficient
CT      thrust coefficient
D       rotor diameter
f       frequency
h       height
M       Mach number
n       rotor angular speed
Re      Reynolds number
ts      time step
$\lambda_2$      lambda-2 vortex criterion

## 2. INTRODUCTION

The Urban Air Mobility (UAM) has been drastically evolving in recent years due to the advent of disruptive new technologies that are enabling Electric Vertical Take-Off and Landing (eVTOL) vehicles. These vehicles are expected to be used for a wide range of applications such as air taxis, package-delivery, emergency services, sovereign functions, agriculture among other possibilities. Rotors, propellers or prop-rotors will drive such concepts. These propulsion systems will significantly change the aerodynamics of the aircraft depending on their characteristics and position all over the airframe. One of the cause of this new aerodynamic behaviour is the propeller wake interaction with the airframe, causing a load rebalance coupled with an unsteady loading. Thus, the overall performance and safety of the aircraft will be very dependent upon the propulsion systems positioning and characteristics. Distributed electric propulsion and wingtip-mounted propeller have many benefits such as reducing the drag of a wing and increasing its lift [1-3].

The aerodynamic design cycle of a wingtip-mounted propeller system usually starts with individual component low-fidelity computational fluid dynamic (CFD) simulations: wing and propeller. The low-fidelity models are utilized to reduce the design space to a manageable number of wing candidates and propeller candidates, which can then be integrated and evaluated

together with a higher-fidelity model. Ultimately, the optimized wingtip-mounted propeller system will be manufactured and tested in a wind tunnel facility.

Since a large part of the design phase of such a system will rely on various fidelity simulation models, it is key ~~to be able~~ to validate these models and know their level of accuracy.

Unfortunately, there is a lack of publicly available experiments of wingtip-mounted propeller to be used publicly for validation purposes.

As part of an initiative to enable the progress in the area of propeller aerodynamics, the Workshop for Integrated Propulsion Prediction (WIPP) provided a set of publicly available experimental data for a wingtip-mounted propeller [4-5]. Different CFD codes have been used to simulate the WIPP benchmark, that includes a high-order potential flow method, RANS models with actuator disks, URANS models with transient sliding meshes and even more sophisticated methods such as enhance delayed detached eddy simulation [6-8].

The main objective of this study is to demonstrate that the Lattice-Boltzmann based solver employed, SIMULIA PowerFLOW, can provide accurate aerodynamic results for a wingtip-mounted propeller configuration. The extensive set of experimental measurement data available will be used and compared to high-fidelity CFD simulations, with truly rotating propellers. SIMULIA PowerFLOW has been previously validated for aerodynamic applications relevant to this work, such as airframe high lift benchmark [9-10], helicopter rotor [11], and rotor wake interaction [12].

The next sections of the present study are organized as follows: First, the wind tunnel facility and model used to measure the reference data will be introduced. Second, information about the solver formulation and simulation models will be shared. Then, simulation results and comparisons against experimental data will be discussed. Finally the main findings and way forwards will be discussed in the conclusion.

## 3. EXPERIMENTAL METHODOLOGY

### 3.1. Wind tunnel

The experimental data used as a reference in this work were measured at Lockheed Marietta Low-Speed Wind Tunnel (LSWT). This facility was selected due to the extensive powered testing experience from previous campaigns. The wind tunnel section is 23:25 feet wide, 16:25 feet high and 43 feet long. The root and floor are parallel, while the sidewalls are slightly divergent, in order to account for the boundary layer growth. The uncertainty levels of the LSWT balance system is very low and for the present case, it is nearly negligible [13].



*Figure 1. LSWT wind tunnel picture, including the wing, the nacelle, the propeller, the wind tunnel walls and the measurement devices. [13]*

### 3.2. Model

The wingtip-mounted propeller model used during the test campaign consists of a tapered wing with a nacelle mounted on its tip. The total span from the tunnel floor to the top of the nacelle is 69.75 inches, which already accounts for a 7 inches long boundary layer splitter plate mounted to the tunnel floor. In addition, the model has an aileron which could be deflected with 45° of amplitude.

The system is powered by an electric motor, which is equipped with an existing C-130 four-bladed 16.2 inches diameter propeller seen on Figure 2 [13]. To increase the experiments repeatability, the wing has been tripped with two layers of 0.25-inch wide tape resulting in a trip height of 0.0125 inch. The trip has been placed at 10% of the local chord on the pressure and suction side of the wing.



*Figure 2. 10%-scale C-130 4-bladed propeller [13]*

### 3.3. Measurement protocol

During the test campaign, the freestream Mach number varied from 0.04 to 0.11, the angle of attack (AoA) of the wing varied from -10° to +20° and the propeller coefficient of thrust (CT) varied discretely from 0.04 to 0.4. To keep a constant CT for the powered-wing during the AoA sweep, the RPM of the propeller were adjusted. Additionally, an unpowered-wing configuration have been tested for the same set of angle of attacks and Mach numbers to compare the two configurations and validate the aerodynamics efficiency benefits of a wingtip-mounted propeller.

Static pressure taps were integrated in the model at six different span wise positions along the wing, as shown in Figure 6. Each row has sixteen taps, carefully positioned to allow a detailed measurement of the pressure variation along the gradient regions. The wing, nacelle and propeller are mounted on a balance that measures the absolute lift and drag of the full system. The balance uncertainty for the lift is 0.37 pounds and the drag uncertainty is 0.045 pounds. The operating conditions used in this paper are: Mach = 0.08, dynamic pressure q = 9.68 psf, chord-based Reynolds number $Re_{MAC}$ = 480265.

The propeller thrust coefficients used are CT=0 for the unpowered-wing and CT=0.4 for the powered-wing. The angle of attack used are: [0°, 5°, 10°, 15°]

### 4. NUMERICAL APPROACH

### 4.1. Lattice-Bolzman Method

The Lattice-Boltzmann Method (LBM) based solver PowerFLOW developed by SIMULIA is used to compute the unsteady flow field. Lattice-based methods are intrinsically explicit, transient and compressible. They are an alternative to traditional CFD methods based on the discretization of the Navier-Stokes equations and derived variations. The basic idea of LBM is to track the advection and collisions of fluid particles from a statistical standpoint. To do so, the particle distribution function f representing the chances that particles in a given volumic cell (voxel) at a specific time adopt a certain velocity vector is resolved. Since it cannot be resolved for an infinity of velocity vectors, the space of possible directions is discretized with an appropriate set of velocity vectors $c_i$, leading to the resolution of the same amount of particle distribution functions $f_i$. Such as in statistical physics, the flow variables such as density and velocity are determined by taking the appropriate moments, i.e. summations over the set of discrete directions of the particle distribution function. A mathematical framework of the LBM has been established by Shan et al. [14] by projecting the distribution function on a basis of Hermite polynomials and computing the moments over the discrete set of particle velocities using Gaussian quadrature formulas for different lattices. In the present work, we make use of

a 19-state lattice, usually referred to as D3Q19. The current version of the solver implements an advanced two-relaxation-time collision operator [15] with Galilean invariance for thermal flows of non-unitary Prandtl number. The operator is also regularized, reducing the aliasing effects due to ghost unresolved moments on the employed lattice [16] and resulting in higher accuracy and improved stability. Rotating geometries can be simulated by resolving the Lattice-Boltzmann equation in the rotating reference system and treating the non-inertial forces as external body forces [17].

### 4.2. Computational setup

A single wind tunnel operating point is considered in this study: M=0.08 with ambient temperature and pressure replicating the experimental conditions. All the external surfaces of the full experimental model have been digitally scanned and converted to a STEP file. This file is the exact digital twin of the model tested. All the geometrical details of the model are maintained in the simulation model, and no simplifications have been made to ensure the prediction's accuracy. Figure 3, shows the CAD model where the blades, spinner, nacelle, wing, aileron can be depicted. All parts of the model are considered rigid and their nominal shapes are used.
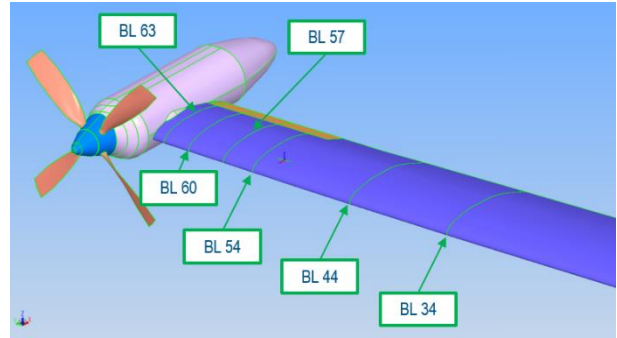


*Figure 3. CAD model of the wingtip-mounted propeller and the wing including the 6 spanwise static pressure measurements*

Two different models are created to investigate the effect of wingtip-mounted propellers. The first case labelled: "NO PROP" or "np" or "unpowered-wing" is composed of the wing, the nacelle and the spinner. The second labelled: "PROP" or "rpm" or "powered-wing" is the exact same setup with the addition of the 4 rotating blades. A single operating point for the propeller is simulated: CT=0.4. Since the CT varies with the AoA of the full system, the RPM is adjusted for each AoA to mimic exactly the experiments. Figure 4 visualize the two different cases.

Figure 4. Simulation models. Unpowered-wing: CT =0 " NO PROP" (left) and powered-wing: CT =0.4 PROP (right)

For each AoA, the exact experimental RPM has been simulated. Four different angle of attacks are studied. Table 1 reports the simulation parameters and the naming convention of the runs. As an example, "C2R0_np" stands for case version 2, resolution 0, no propeller. Version 3 is a cost optimised setup of version 2 keeping the same accuracy.

Table 1. Simulated cases

| Run | Tripped airframe | Prop blades | RPM | CT | a0a |
|---|---|---|---|---|---|
| C3R0_rpm | No | Yes | 5856 | 0.4 | 0 |
| C3R0_rpm | No | Yes | 5820 | 0.4 | 5 |
| C3R0_rpm | No | Yes | 5808 | 0.4 | 10 |
| C3R0_rpm | No | Yes | 5760 | 0.4 | 15 |
| C2R0_np | No | No | 0 | 0 | 0 |
| C2R0_np | No | No | 0 | 0 | 5 |
| C2R0_np | No | No | 0 | 0 | 10 |
| C2R1_np | No | No | 0 | 0 | 0 |
| C2R1_np | No | No | 0 | 0 | 5 |
| C2R1_np | No | No | 0 | 0 | 10 |
| C3R0_np | No | No | 0 | 0 | 0 |
| C3R0_np | No | No | 0 | 0 | 5 |
| C3R0_np | No | No | 0 | 0 | 10 |
| C3R0_np | No | No | 0 | 0 | 15 |
| C3R0_np_T | Yes | No | 0 | 0 | 10 |
| C3R0_np_T | Yes | No | 0 | 0 | 15 |

The computational domain is subdivided into numerous variable resolution volumes. It is discretized with a Cartesian isotropic mesh using a cut-cell approach at the wall. Figure 5 shows the different meshing strategies used around the wing profile. Solid walls with, pressure and velocity inlet boundary condition, pressure outlet boundary condition and no slip sidewalls bind the computational volume. A sponge zone strategy is also used to prevent pressure waves from re-entering the computational domain. Each cases is run for 20 full propeller revolutions and the measurements are sampled for the last 6 revolutions. To reach statistical convergence of the flow faster, the simulation is initialized with the aerodynamic field from the last time-step of a coarser simulation. The coarse simulation has larger voxels, which greatly reduces the computational time while keeping the same physical time: 20 full propeller rotations.
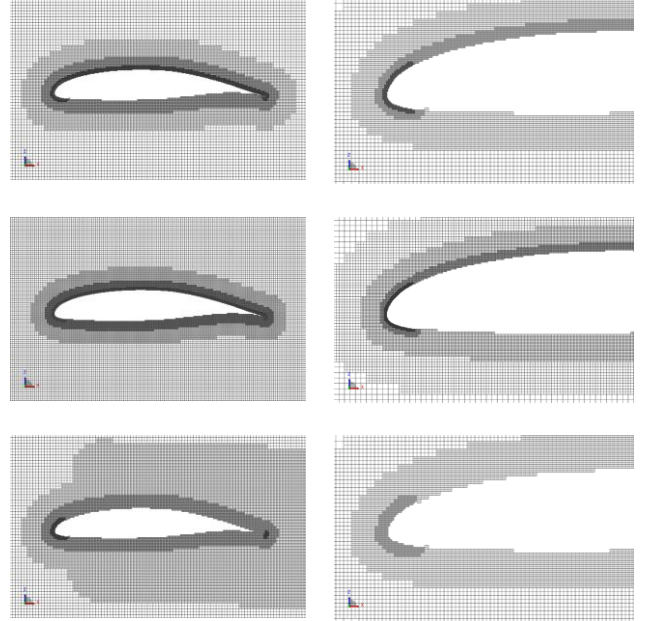


Figure 5. Cartesian volume mesh around the wing. From top to bottom: C2R0, C2R1, C3R0 cases. From left to right: full span, leading edge close-up

Each simulation has been run on a 479 cores rack clocked at 2.9 GHz. Table 2 reports the total number of voxels, surfels and simulation hours of each simulations.

Table 2. Computational grid and simulation cost

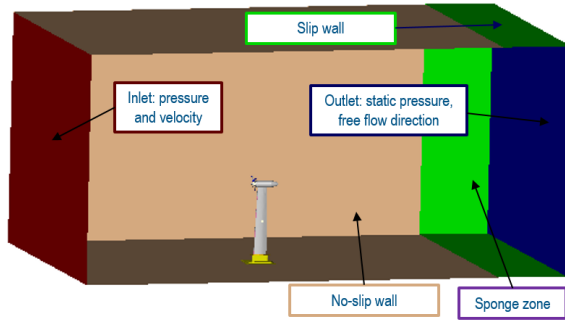| Runs | Voxel | Surfel | cpuh |
|---|---|---|---|
| C2R0_np | $3.7 \times 10^8$ | $8.1 \times 10^6$ | $3.3 \times 10^3$ |
| C2R1_np | $8.6 \times 10^8$ | $1.5 \times 10^7$ | $12.8 \times 10^3$ |
| C3R0_np | $3.2 \times 10^8$ | $3.4 \times 10^6$ | $2.8 \times 10^3$ |
| C3R0_np_T | $6.9 \times 10^8$ | $5.3 \times 10^7$ | $61.7 \times 10^3$ |
| C3R0_rpm | $3.4 \times 10^8$ | $6.3 \times 10^6$ | $3.1 \times 10^3$ |

Figure 6. Schematic of the full simulation domain

## 5. RESULTS

In this study, only Mach 0.08 and CT = 0.4 conditions have been considered. Run 27 correspond to the powered-wing experiment at CT = 0.4 and Run 180 correspond to the unpowered-wing experiment.

### 5.1. Resolution study

Figure 7 shows the grid convergence polar of the lift coefficient for the model: "NO PROP". Three different and equally spaced AoA were tested: 0, 5 and 10°, to cover a wide range of flow topologies. For 0°, C2R0_np and C2R1_np results are nearly identical, showing good grid convergence. However, when the AoA increases and thus the flow starts to separate on the suction side of the wing, the results tend to differ.
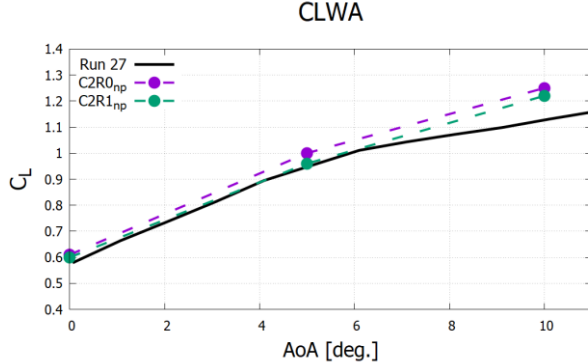


Figure 7. Lift coefficient function of angle of attack: unpowered-wing. Run 27 correspond to the powered-wing experiment at CT = 0.4.

With Figure 8, two phenomena can be seen: the first one is that for higher angle of attack, the velocity gradient at the leading edge is greater. The second is for higher angle of attack the flow is separated on the suction side toward the trailing edge.
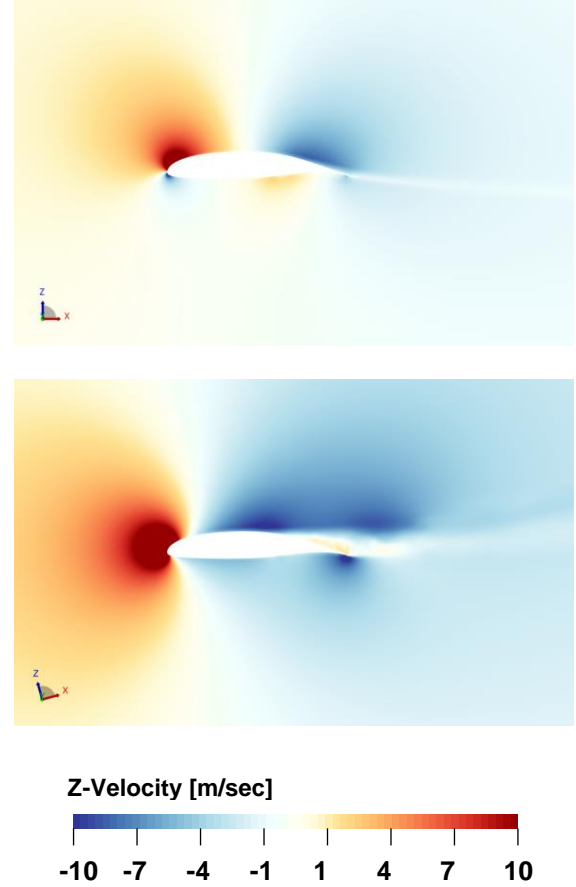


Figure 8. Time averaged snapshot of the Z-Velocity at mid-span. C3R0_np AoA 0° (Top) and C3R0_np AoA 15° (Bottom)

With finer resolution, you capture the boundary layer better and can rather capture the onset of flow reversal near the wall. Then with finer resolution, you can better predict the leading edge flow acceleration resulting in a higher suction peak, leading to a steeper pressure recovery, causing more velocity deficit in the boundary layer that will lead to earlier separation. A separation generates a broad range of vortex sizes and increasing the resolution in this area helps to resolve the smaller vortex scales. When the angle of attack increases, the curvature seen by the flow at the leading edge rises and so is, the pressure gradient. These points explain why having a higher resolution will help to correlate better for higher angle of attacks.

### 5.2. Comparison simulation vs experiments

The first set of results focuses on the validation of the propeller thrust. The tested thrust coefficient CT was 0.4 and kept constant during the AoA sweep. The CT is defined as:

$$CT = \frac{T}{q.S_{ref}}$$

5

Where T is the propeller thrust, q is the free-stream dynamic pressure and Sref is the wing planform area. Table 3 presents the rotor's aerodynamic results of case: "PROP". The agreement with the CT between tests and simulation is excellent with a maximum error of 3.1% for 15° of AoA.

*Table 3. Validation of propeller aerodynamics data*

| AoA | RPM | Thrust [lb] | $CT_{sim}$ | $\Delta CT_{sim-exp}$ |
|---|---|---|---|---|
| 0 | 5856 | 18.53 | 0.408 | 2.0% |
| 5 | 5820 | 18.35 | 0.404 | 1.0% |
| 10 | 5808 | 18.61 | 0.410 | 2.4% |
| 15 | 5760 | 18.73 | 0.413 | 3.1% |

Next validation results focus on the wing surface pressure at six span-wise locations. Figure 3 shows the pressure tap locations. Figure 7 reports the simulation surface pressure coefficient and experimental wing pressure taps for the powered-wing: "PROP" case. Cp is defined as:

$$Cp = \frac{p - p_0}{q}$$

Where p is the wing surface static pressure, $p_0$ is the ambient static pressure and q is the free-stream dynamic pressure.

In general, a very good agreement between experiments and simulation can be seen. Three main features of the flow are captured in the simulation and in the experiments. First, the suction peaks amplitudes increase with the angle of attack. Second, BL 57 and BL 60 have higher suction peaks. Third, for angle of attack 10° and 15° a smooth body separation is happening on the suction side of the wing for all the BL except for BL 60. The first flow feature is explained with Figure 8, the greater the angle of attack is, the higher the velocity and the velocity gradient are on the suction side of the wing close to the leading edge. This leads to a greater suction peak. Figure 8 gives insights to explain the second flow feature. As one can observe, the propeller slipstream affects considerably the wing static pressure distribution, by changing the local velocity vector. The propeller is accelerating the flow and increasing the effective angle of attack seen by the wing. This results in a greater suction peak. BL 60 is thus seeing a faster flow with a higher angle of attack than the other BL station and is the only one not separated. To explain this third flow feature, Figure 9 highlights the vorticity magnitude around the wing profile. It can be seen that the boundary layer of the wingspan immersed in the propeller slipstream is more turbulent than the one of the clean wing and thus, the former stays attached for a longer chord position. This explains why even with a higher angle of attack and higher speed this wingspan stays attached.



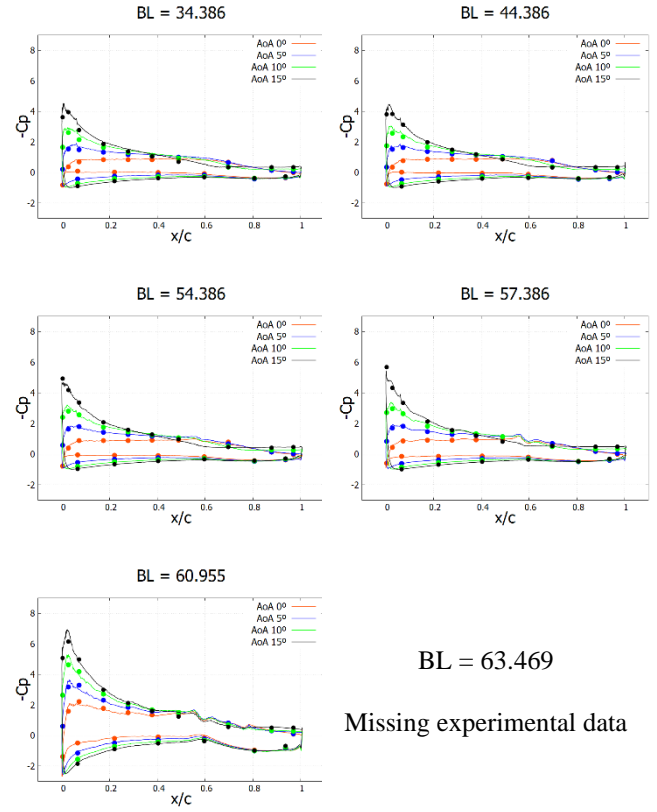BL = 63.469

Missing experimental data

*Figure 7. Validation of surface pressure data: powered-wing "PROP" for different span-wise positions and AoA. Simulation is represented with plain lines and experiments with circles*
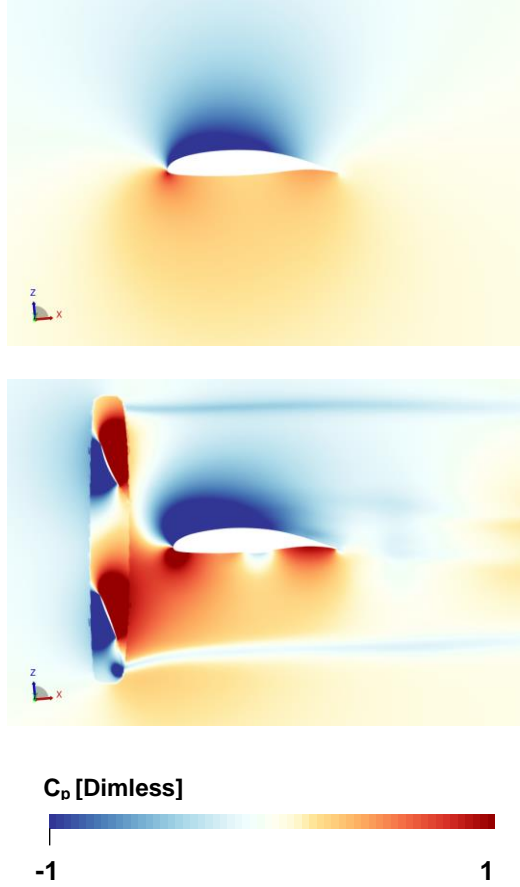
**C_p [Dimless]**

**-1**                          **1**

*Figure 8. Time averaged snapshot of Cp for case C3R0_RPM AoA 5°. Mid-span slice (Top) and tip slice (Bottom)*



**Vorticity Magnitude [dimless]**
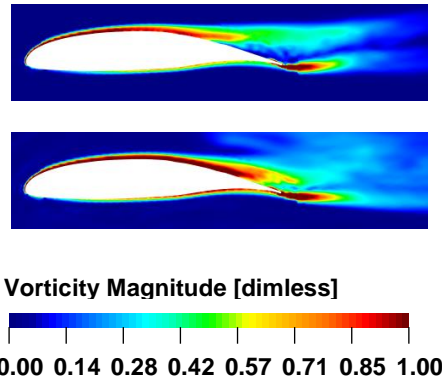
**0.00 0.14 0.28 0.42 0.57 0.71 0.85 1.00**

*Figure 9. Time averaged snapshot of Vorticity magnitude. Slice position at the tip of the wing, behind the propeller. C3R0_np AoA 15° (Top) and C3R0_RPM AoA 15° (Bottom)*

Then, next validation results focuses on the unpowered-wing: "NO PROP" case. Figure 10 reports the simulation surface pressure and experimental wing pressure taps this time for the cases without the propeller. As discussed in the previous paragraph, the agreement is in general very good.
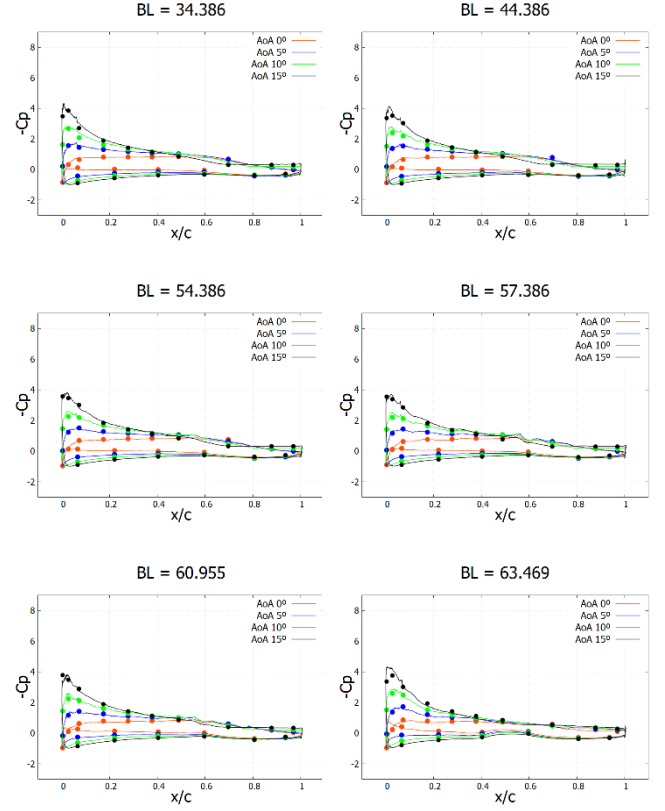


*Figure 10. Validation of surface pressure data: unpowered-wing "NO PROP" for different span-wise positions and AoA. Simulation is represented with plain lines and experiments with circles*

Instantaneous volume flow visualization of $\lambda_2$ criterion in Figure 11 shows the flow separation taking place on the suction side of the wing. The propeller tip vortex and wake are interacting with the wing and then with the wake of the wing. The large structures are breaking down into smaller structures. The tip vortex of the wing is rotating in the opposite direction of the rotor slipstream. Figure 12 highlights the shear layer between the wing tip vortex due to the lift of the wing and the rotor slipstream. This interactional mechanism results in a smaller wing tip vortex, which results in lower induced drag.
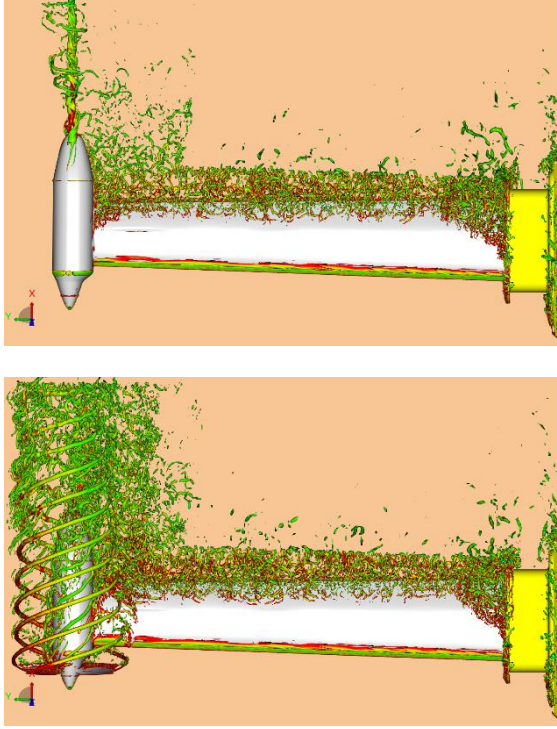
*Figure 11. Instantaneous snapshot of $\lambda_2$ criterion iso-surfaces colored by vorticity magnitude. C3R0_np AoA 15° (Top) and C3R0_RPM AoA 15° (Bottom).*
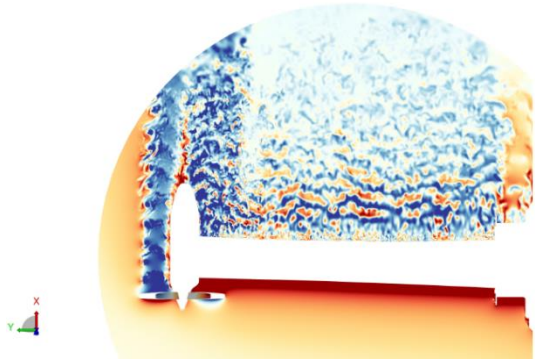


*Figure 12. Instantaneous snapshot of Z-velocity C3R0_RPM AoA 15°*

Next validation results are focused on the integrated overall forces: drag and lift. Simulated drag polar are compared with measured data for both cases: "PROP" and "NO PROP" in Figure 13. The $C_D$ is defined as:

$$C_D = \frac{Drag}{q.S_{ref}}$$

Where Drag is the integrated drag force, q is the free-stream dynamic pressure and $S_{ref}$ is the wing planform area.

The correlation of the drag coefficient is in excellent agreement. For each angle of attack simulated, the results are perfectly on top of the experiments. The CFD-RANS FUN3D results [18] also compare well with the reference data, even if the drag coefficients are slightly under-predicted, which could mean a higher propeller thrust. The effect of the propeller on the overall drag forces can be noticed by two different trends. First, the results generated by the PROP configuration, which is represented in this picture by the green curve, are shifted down, compared to the NO PROP configuration, represented by the purple colour. This is due to the thrust force generated by the 4-bladed propeller.

Additionally, shape of the PROP curve is gradually changing from linear to a slightly parabolic curve, as the AoA increases. This means that at higher angle of attacks, the propeller is losing its effect and generating more and more drag as the angle of attack of the full system is increasing. The NO PROP curve, on the other hand, shows a more linear shape.
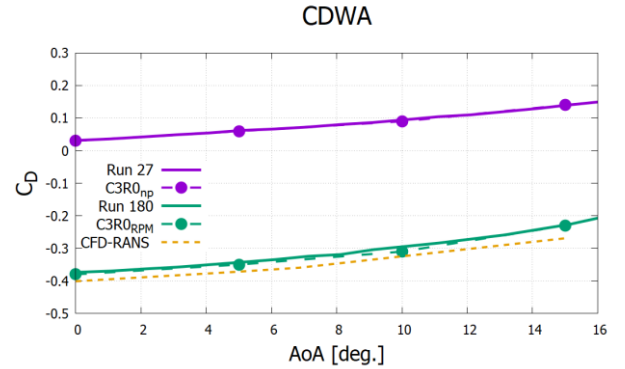


*Figure 13. Validation of drag coefficient function of angle of attack. Run 27 correspond to the powered-wing experiment at CT = 0.4 and Run 180 correspond to the unpowered-wing experiment.*

For the lift coefficient, Figure 14 shows the comparison of the simulation and the experiments for both configurations. The $C_L$ is defined as:

$$C_L = \frac{Lift}{q.S_{ref}}$$

Where Lift is the integrated lift force, q is the free-stream dynamic pressure and $S_{ref}$ is the wing planform area.

In general, the correlation is good for both cases: "PROP" and "NO PROP". However, around 10° of angle of attack, the simulation is consistently overestimating the lift coefficient. A large smooth body separation is starting above 5°, as observed in the previous paragraph. The simulation did capture the smooth body separation at such low AoA but it under-predicted it. Other CFD codes, such as FUN3D [18], which is based on the RANS formulation with uniform thrust actuator disk, also over-

predicted lift at mid to high AoA. The discrepancy becomes even more pronounced as the angle of attack increases. Up to 10°, both software provided very similar trends. However, at 15°, when the wing is strongly separated, the current results present a better correlation with the experimental data, with a correct capture of the separation confirming the advantage of the scale-resolving approach for massively separated flows.
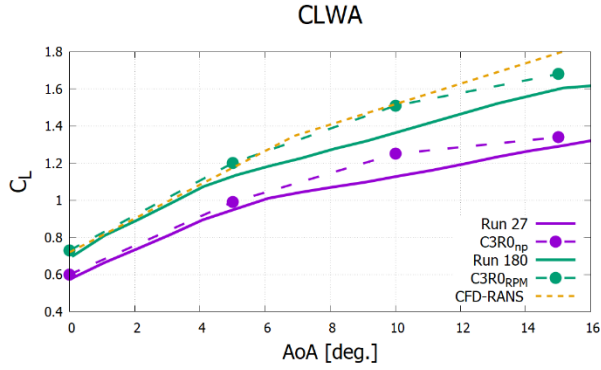


Figure 14. Validation of lift coefficient function of angle of attack. Run 27 correspond to the powered-wing experiment at CT = 0.4 and Run 180 correspond to the unpowered-wing experiment.

Looking at the overall shape of the curves, it can be seen the effect of the wing-tip mounted propeller is increasing the amplitude of the lift coefficient for all the angle of attacks. However, the propeller is not cancelling the smooth body separation since the slipstream of the propeller is only blowing a small portion of the wing.

The propeller slip-stream is not only influencing the part of the wing right behind the propeller, it is also influencing the part of the wing in its vicinity. Figure 15 shows the Cp cuts for BL 57 and BL 60. The flow speed and angle of attack seen by the blown wing at BL 57 is higher than the NO PROP case. However, the flow is not more turbulent so this is not delaying the separation. This is actually the opposite, the PROP case separates a bit earlier than the NO PROP case.
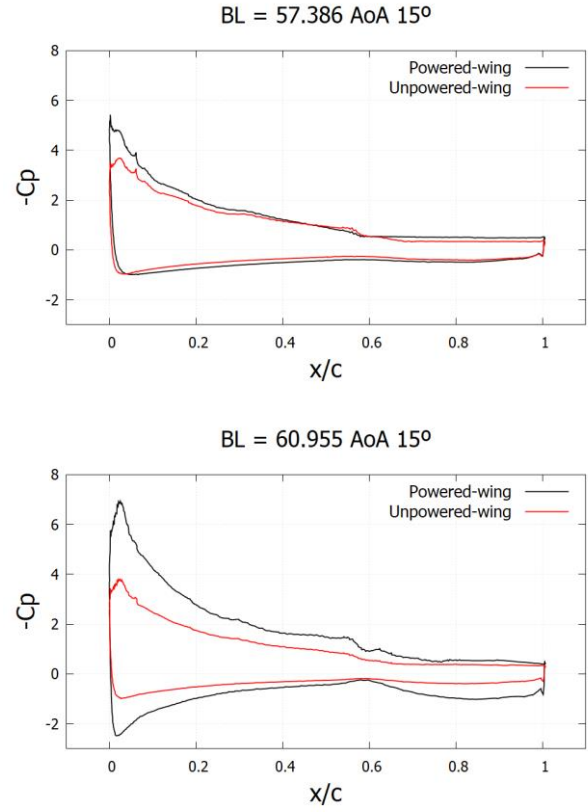


Figure 15. Surface pressure data of powered and unpowered-wing cases for AoA 15° at two different span-wise positions. Out of the propeller slipstream (Top) and in the propeller slipstream (Bottom)

Similar conclusion can be drawn looking at Figure 16 and Figure 17 showing the z-velocity on the suction side of the wing. The flow is separating earlier for the PROP cases except for BL 60 which is seeing the additional turbulent content.
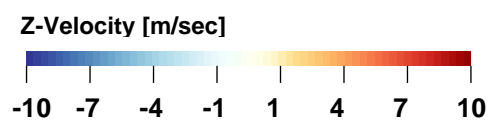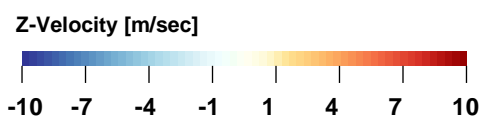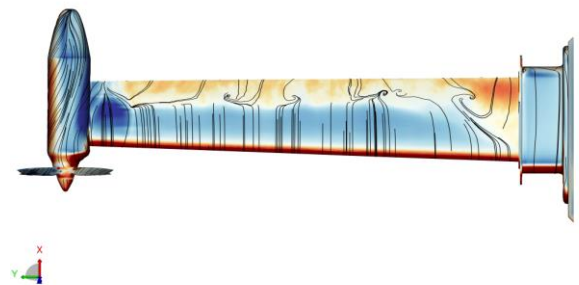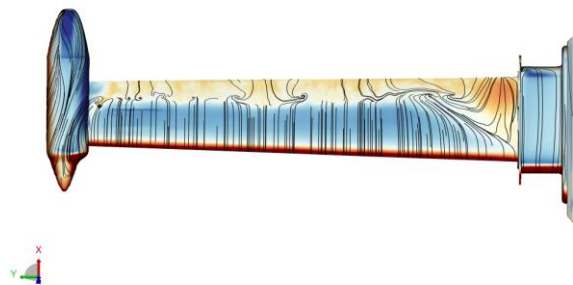
**Z-Velocity [m/sec]**

-10  -7  -4  -1  1  4  7  10
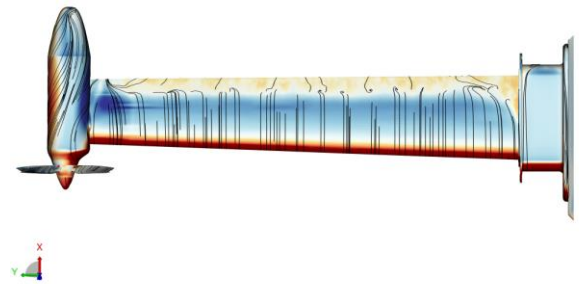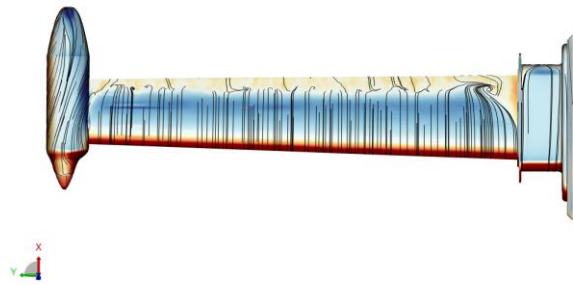
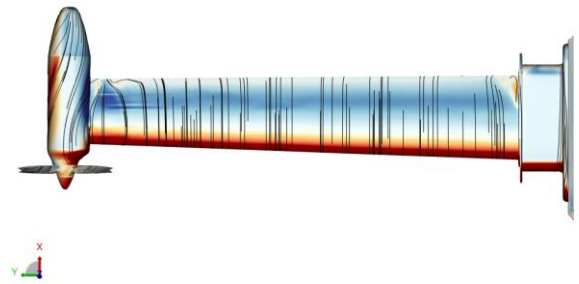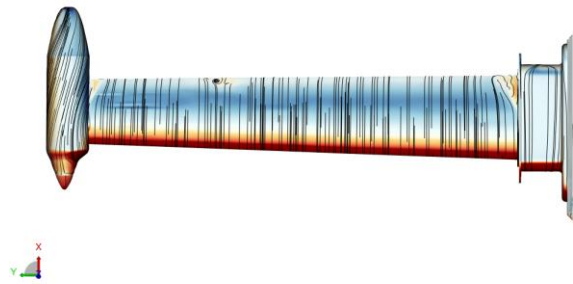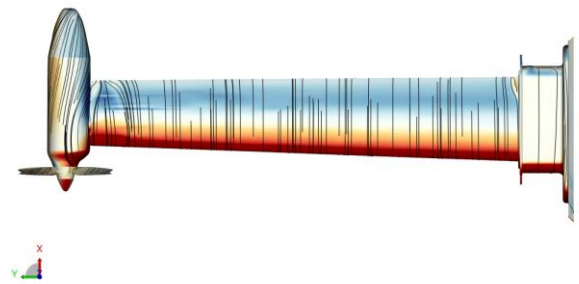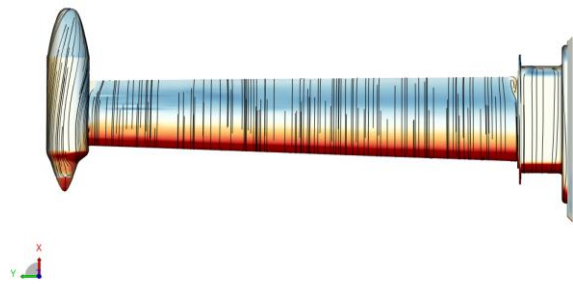*Figure 16. Surface Z-velocity C3R0_np AoA sweep: 0° to 15°*

**Z-Velocity [m/sec]**

-10  -7  -4  -1  1  4  7  10

*Figure 17. Surface Z-velocity C3R0_RPM AoA sweep 0° to 15°*

### 5.3. Trip sensitivity study

Since during the tests the wing has been tripped on the suction and pressure side, a similar trip geometry has been added to the simulation model of the "NO PROP" case to allow a fair comparison with the experiments. Figure 18 shows the effect of the trip on the simulation results. It can be seen that with the trip, the lift coefficient is in a better agreement with the experiments. By including a physical trip, the solver is forced to an under-resolved LES mode within the boundary layer. Having a wall law enables to captures the anisotropic turbulent structures of the boundary layer and its dynamics that are key in smooth body separation cases. However, despite the better trends provided by the inclusion of the trip, the lift coefficient is still over-predicted at 10°. This could be explained by an under-resolved boundary layer or a limit of the wall-model used.
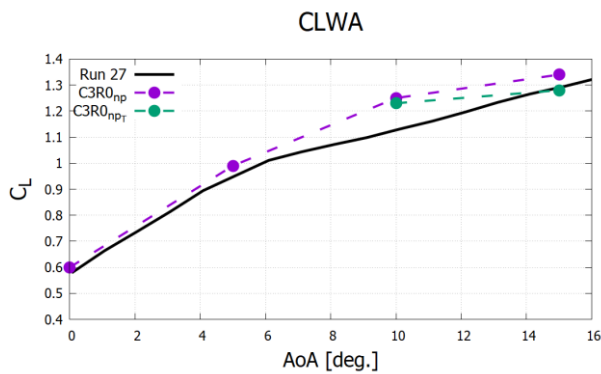


*Figure 18. Lift coefficient function of angle of attack. Run 27 correspond to the powered-wing experiment at CT = 0.4.*

## 6. CONCLUSION

In this study, SIMULIA PowerFLOW has been applied to the 1ˢᵗ AIAA Workshop: WIPP. The obtained results with PowerFLOW showed overall good agreement with the experimental data. The wing pressure distributions were accurately predicted for all span-wise sections and conditions. The smooth body separations taking place on the suction side of the wing for AoA > 5° were captured. The drag coefficients are in excellent agreement with the experimental data, which is a good indication that the propeller aerodynamics was well resolved for the powered-wing. The lift coefficients are in excellent agreement with the experimental data for AoA 0° and 5°. For AoA 10° and 15° the lift coefficients are overestimated. The inclusion of the trip improved the lift coefficient prediction. More resolution downstream the trip would be necessary to properly resolve the flow structures introduced by the trip to improve the lift prediction. The effects of the wingtip-mounted-propeller were discussed. The slipstream of the propeller increases the apparent AoA and the dynamic pressure of the wingspan immersed in it. Additionally, due to the increase of turbulent kinetic energy generated by the

rotating blades, it delays the separation of the flow. This results in higher lift for the powered-wing compared to the unpowered-wing for all the simulated AoA.

## 7. REFERENCES

1. Sinnige, T., van Arnhem, N., Stokkermans, T. C. A., Eitelberg, G., and Veldhuis, L. L. M., "Wingtip-Mounted Propellers: Aerodynamic Analysis of Interaction Effects and Comparison with Conventional Layout," Journal of Aircraft, Vol. 56(1), 2018, pp. 295–312. doi:10.2514/1.C034978.

2. Moore, M. D. (2014). Misconceptions of electric aircraft and their emerging aviation markets. In 52nd Aerospace Sciences Meeting (p. 0535).

3. Stoll, A. M., Bevirt, J., Moore, M. D., Fredericks, W. J., & Borer, N. K. (2014). Drag reduction through distributed electric propulsion. In 14th AIAA aviation technology, integration, and operations conference (p. 2851).

4. Starr, G., Schiltgen, B., Hooker, R., and Wick, A. (2019). Workshop for Integrated Propeller Prediction (WIPP) from AIAA Aviation Forum and Exhibit - Presentation.

5. Wind Tunnel Testing of Propeller Wingtip Interactions, Tech. rep., NASA SBIR Phase III Final Report, 2019.

6. Cole, Julia & Barcelos, Devin & Krebs, Travis & Melville, Michael & Bramesfeld, Götz. (2020). Prediction of WIPP Data using a Relaxed-Wake Potential Flow Method. 10.2514/6.2020-2681.

7. Baruzzi, Guido & Aliaga, Cristhian & Ozcer, Isik & Stokes, John & Svihla, Kurt & Saxena, Swati. (2020). Numerical Simulation of an Integrated Propeller with Models of Progressively Increasing Fidelity. 10.2514/6.2020-2682.

8. Zhou, Beckett & Morelli, Myles & Gauger, Nicolas & Guardone, Alberto. (2020). Simulation and Sensitivity Analysis of a Wing-Tip Mounted Propeller Configuration from the Workshop for Integrated Propeller Prediction (WIPP). 10.2514/6.2020-2683.

9. Rumsey, C. L., Slotnick, J. P., & Sclafani, A. J. (2019). Overview and summary of the third AIAA high lift prediction workshop. Journal of Aircraft, 56(2), 621-644.

10. Ihi, R., Ribeiro, A., Santos, L., and Silva, D., "Lattice Boltzmann Simulations of Flow Over an Iced Airfoil," SAE Technical Paper 2019-01-1945, 2019

11. van der Velden, W. C. P., Romani, G., & Casalino, D. (2021). Validation and insight of a full-scale S-76 helicopter rotor using the Lattice-Boltzmann

Method. Aerospace Science and Technology, 118, 107007.

12. Gonzalez-Martino, I., Romani, G., Wang, J., & Casalino, D. (2018). Rotor Noise Generation in a Turbulent Wake using Lattice-Boltzmann Methods. In 2018 AIAA/CEAS Aeroacoustics Conference (p. 3447).

13. Hooker, John & Wick, Andrew & Ginn, Starr & Walker, Jimmy & Schiltgen, Benjamin. (2020). Overview of Low Speed Wind Tunnel Testing Conducted on a Wingtip Mounted Propeller for the Workshop for Integrated Propeller Prediction. 10.2514/6.2020-2673.

14. Shan, X., Yuan, X.-F. and Chen, H. "Kinetic theory representation of hydrodynamics: a way beyond the Navier Stokes equation", Journal of Fluid Mechanics, 2006, 550, 413-441.

15. CHEN, H., GOPALAJRISHNAN, P., ZHANG, R. (2004). Recovery of Galilean Invariance in Thermal Lattice Boltzmann Models for Arbitrary Prandtl Number. International Journal of Modern Physics C 25(10).

16. Zhang, R., Shan, X. and Chen, H. "Efficient kinetic method for fluid simulation beyond the Navier-Stokes equation Physical", Review E, American Physical Society, 2006, 74, 046703.

17. Zhang, R., Sun, C., Li, Y., Satti, R., Shock, R., Hoch, J., and Chen, H., "Lattice Boltzmann approach for local reference frames,"Communications in Computational Physics, Vol. 9, No. 5, 2011, pp. 1193–1205.

18. Nicolas Reveles, Kyle Seledic, Darryl Williams, Eric Blades and Parthiv N. Shah. "Rotor/Propeller Model Fidelity Effects on Propeller-Wing Interactional Aerodynamics," AIAA 2020-2676. AIAA AVIATION 2020 FORUM. June 2020.